Title

Room-Temperature, Current-Induced Magnetization Self-Switching in A Van Der Waals Ferromagnet

Journal

Advanced Materials, 36(9)

ISSN

0935-9648

Authors

Zhang, Hongrui

Chen, Xiang

Wang, Tianye

et al.

Publication Date

2024-03-01

DOI

10.1002/adma.202308555

Peer reviewed

Room-temperature, current-induced magnetization self-switching in a van der Waals ferromagnet

Hongrui Zhang[#,], Xiang Chen[#], Tianye Wang[#], Xiaoxi Huang, Xianzhe Chen, Yu-Tsun Shao, Fanhao Meng, Peter Meisenheimer, Alpha N'Diaye, Christoph Klewe, Padraic Shafer, Hao Pan, Yanli Jia, Michael F. Crommie, Lane W. Martin, Jie Yao, Ziqiang Qiu, David A. Muller, Robert J. Birgeneau, Ramamoorthy Ramesh[*]*

H. R. Zhang, X. X. Huang, X. Z. Chen, F. H. Meng, P. Meisenheimer, H. Pan, Y. L. Jia, L. W. Martin, J. Yao, R. Ramesh
Department of Materials Science and Engineering,
University of California, Berkeley,
CA, 94720, USA.
Email: hongruizhang@berkeley.edu, rramesh@berkeley.edu
H. R. Zhang, X. Chen, X. Z. Chen, F. H. Meng, M. F. Crommie, L. W. Martin, J. Yao, R. J. Birgeneau, R. Ramesh
Materials Sciences Division,
Lawrence Berkeley National Laboratory,
Berkeley, CA, 94720, USA
X. Chen, T. Y. Wang, M. F. Crommie, Z. Q. Qiu, R. J. Birgeneau, R. Ramesh
Department of Physics,
University of California,
Berkeley, CA, 94720, USA.
Y. T. Shao, D. A. Muller
School of Applied and Engineering Physics,
Cornell University,
Ithaca, NY, USA.
A. N'Diaye, C. Klewe, P. Shafer
Advanced Light Source,
Lawrence Berkeley National Laboratory,
Berkeley, CA 94720, USA
D. A. Muller
Kavli Institute at Cornell for Nanoscale Science,
Cornell University,
Ithaca, NY, USA
R. Ramesh
Department of Physics and Astronomy, Department of Materials Science and Nanoengineering,
Rice University,
Houston, 77005, TX, USA
[#]These authors contributed equally: Hongrui Zhang, Xiang Chen, Tianye Wang.

Keywords: current-induced magnetization self-switching, spin-orbit torque, van der Waals materials, room temperature, polar magnet.

Abstract

Two-dimensional layered materials with broken inversion symmetry are being extensively pursued as spin-orbit coupling layers to realize high-efficiency magnetic switching. Such low-symmetry layered systems are, however, scarce. In addition, most layered magnets with perpendicular magnetic anisotropy show a low Curie temperature. Here, we report the experimental observation of spin-orbit torque magnetization self-switching at room temperature in a layered polar ferromagnetic metal, $Fe_{2.5}Co_{2.5}GeTe_2$. **The spin-orbit torque is generated from the broken inversion symmetry along the *c* axis of the crystal. Our results provide a direct pathway toward applicable two-dimensional spintronic devices.**

1. Introduction

Low symmetry in nonmagnetic[1-4] and antiferromagnetic[5-8] materials plays an essential role in generating torques for magnetization switching, rendering the writing functionality in next-generation magnetic memory devices. Self-switching of the magnetization direction by a current without an additional spin-orbit coupled (SOC) layer can be realized in ferromagnets with broken inversion symmetry, such as $Ga_{1-x}Mn_xAs$[9], $Ge_{1-x}Mn_xTe$[10], $L1_0$-FePt[11], CoTb[12,13], FeTb[14], and CoPt[15]. Layered materials can be used to readily construct low-symmetry crystal structures due to the existence of various stacking configurations and atomic occupancies.[16] For example, 2*H*-NbS_2 is a typical transition metal dichalcogenide with no inversion symmetry breaking. In contrast, 3*R*-NbS_2, with a different stacking configuration, is a non-centrosymmetric compound, and $Fe_{1/3}NbS_2$, with iron intercalated between the 2H-NbS_2 layers, exhibits inversion symmetry breaking and antiferromagnetic ordering, which can favor current induced in-plane Néel vector switching.[17] In addition, the highly efficient magnetization switching in a two-dimensional ferromagnetic Fe_3GeTe_2 by bulk SOT can be realized[18-20]. The low symmetry in the Fe_3GeTe_2 system is probably induced by the inhomogeneous occupation of the FeII site [21]. However, most of the SOT-induced magnetization (self-)switching in two-dimensional materials is limited to well below room temperature, thus possibly limiting practical implementation.

The Fe_NGeTe_2 (N = 3, 4, or 5; FGT, N > 3) system has good electrical conductivity, a Curie temperature that approaches, or is higher than, room temperature at N = 5, and widely tunable magnetic anisotropy,[12,22-24] thus making it an ideal candidate system for two-dimensional (2D) spintronic devices. The FGT system exhibits a centrosymmetric structure,

in which the iron atoms can be intercalated between the tellurium and Fe_3Ge layers of Fe_3GeTe_2 to form Fe_4GeTe_2 and Fe_5GeTe_2. The occupancy of the iron atom sites in the FGT system is very sensitive to the iron content and its chemical environment.[25-29] This provides an approach to design atomic ordering and crystal stacking to obtain a room-temperature magnetic metal with broken inversion symmetry. By control of synthesis parameters and stoichiometry, a non-centrosymmetric room-temperature magnetic metal, $Fe_{2.5}Co_{2.5}GeTe_2$ (FCGT), with a C_{6v} (6mm) point group was obtained.[25] (see Figure S1, Supporting Information) The resulting polar structure is induced by the Fe1 site ordering (Figure 1 **a**, **b,)**, and the polar axis is along the *c* axis of the crystal. This new phase of FCGT remains ferromagnetic with a high Curie temperature (350 K).

Due to the Dzyaloshinsky–Moriya interaction (DMI) induced by the polar structure and magnetization with an out-of-plane easy axis, Néel-type skyrmions can be stabilized in this system. In a thick (~ 136 nm) FCGT nanoflake, larger dipolar energy dominates, stabilizing a stripe domain state at remanence and room temperature. (see Figure S2, Supporting Information) Once a non-zero out-of-plane magnetic field is applied, a Néel-type skyrmion lattice is observed. Consequently, by applying a current, it prefers the formation and motion of skyrmions rather than switching to up/down magnetization states.[30] (see Figure S2, Supporting Information) As the thickness of the nanoflake decreases, the large magnetic shape anisotropy leads to a single domain state driving the FCGT to stabilize into two magnetic states (*i.e.*, up and down magnetization) at remanence. (see Figure S3, Supporting Information) Combined with the inversion symmetry breaking of the crystal, the stabilization of two magnetization states allows one to achieve current-induced magnetization self-switching in FCGT at room temperature.

Based on these, in this work, we have successfully achieved current-induced magnetization self-switching at room temperature in a single-layer FCGT device. The SOT is generated by the crystal structure of FCGT with an inversion symmetry breaking along the *c*-axis. The switching processes are highly repeatable at room temperature under various assisted magnetic fields. The effective field induced by current, as estimated by the second harmonic Hall measurements, is 1.4×10^{-5} Oe cm^2/A. FCGT exhibits the potential to serve as a low-dimensional, single-layer, room-temperature SOT-based spintronics device.

2. Structure and room-temperature magnetic properties of FCGT

The experimental device used to probe the FCGT is illustrated (Figure 1**c**), wherein the FCGT nanoflake was transferred onto metal electrodes grown on thermally oxidized silicon

wafers (see Figure S4, Supporting Information). An h-BN layer is used to cap the FCGT layer to avoid its degradation. A schematic of the atomic structure of the FCGT (Figure 1**a**, **b**) reveals that each sublayer stacks in a zigzag fashion along the *c*-axis. The Fe1-site ordering (marked by the solid yellow circles [full occupancy] and open red circles [full vacancy]) induces a polar symmetry breaking along the *c*-axis. The iron/cobalt cations occupy the Fe1,2,3 sites, and there is no obvious vertical composition gradient, introducing additional broken inversion symmetry. This is confirmed by single-crystal X-ray diffraction and high-resolution cross-section scanning transmission electron microscopy (Figure 1**b**).[25] Angle-dependent Raman measurements at room temperature show in-plane isotropy, indicating no lateral low crystal symmetry in the FCGT system (see Figure S5, Supporting Information).

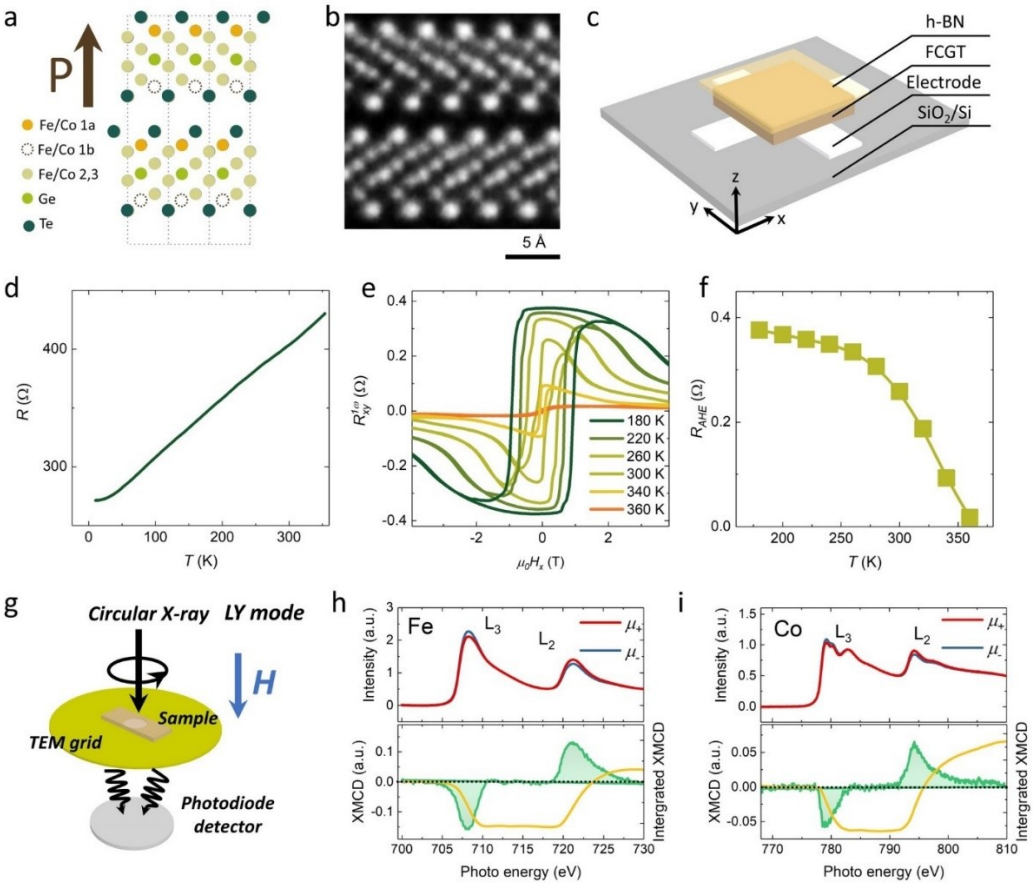

Figure 1 Structure and room-temperature properties of the FCGT flake. a, b) side view of the FCGT crystal structure and the cross-section high-angle annular dark-field STEM (HAADF-STEM) image of the FCGT. c) A schematic image of the FCGT device. d) Temperature-dependent resistance curve for 15-layer FCGT nanoflake, indicating a metallic behavior of the FCGT flake. e) Hall resistance R_{xy} as a function of $\mu_0 H$ at different temperatures. f) The saturated anomalous Hall resistance as a function of temperature. g) The

experimental setup of the XAS. h, i) Element-resolved XMCD measurements from the Fe absorption edge (h) and the Co absorption edge (i) under the magnetic field of 1T.

The room-temperature, macroscopic magnetic properties of the FCGT nanoflakes were characterized by transport measurements. The resistance of the FCGT nanoflakes (15-layers) is almost linearly dependent on temperature (Figure 1**d**); thus, exhibiting a metallic behavior across the entire temperature range studied herein. Temperature-dependent anomalous Hall effect studies of an FCGT nanoflake were measured by sweeping an in-plane magnetic field along the *x*-direction. (Figure 1**e**) These curves exhibit parabolic characteristics at low magnetic fields, which is a typical hard-axis magnetic hysteresis loop for materials with perpendicular magnetic anisotropy. As the temperature increases, the hysteresis gradually disappears, and so does the anomalous Hall resistance, showing a Curie temperature ~ 350 K, see Figure 1**f**. The apparent anomalous Hall curve at 300 K confirms the room-temperature ferromagnetic ordering of FCGT nanoflake.

Macroscopic magnetic measurements show that the FCGT system is a ferromagnet at room temperature. In reality, both the iron and cobalt cations can contribute to the magnetization. In order to investigate the intrinsic magnetic ground state, element-resolved X-ray absorption spectroscopy (XAS) and X-ray magnetic circular dichroism (XMCD) measurements were performed at room temperature. XAS studies were completed in the bulk-sensitive luminescence yield (LY) mode, which can eliminate the influence of a (potentially) oxidized surface layer that contributes to the magnetic signal. The schematic geometry of the XAS/XMCD setup is provided (Figure 1**g**), wherein the FCGT nanoflakes are transferred onto transmission electron microscopy grids with 200 nm silicon nitride windows. The X-rays transmit through the sample in the grid windows, thus providing averaged information from the whole FCGT layer. The XAS (μ^+ and μ^-) spectra at the Fe-$L_{2,3}$ and Co-$L_{2,3}$ absorption edges measured at room temperature for a 60-nm-thick FCGT flake are presented (Figure 1**h** and **i**, respectively). The XMCD manifests as the difference of X-ray absorption spectra, μ^+- μ^-. Clear XMCD signals appear near both the iron and cobalt absorption peaks, suggesting that the ferromagnetism of FCGT originates from the spin polarization of both the iron and cobalt 3*d* electrons. The sign of the Fe-L_2 (Fe-L_3) peak is the same as that of the Co-L_2 (Co-L_3) peak, indicating that iron and cobalt are ferromagnetically coupled. Magnetic hysteresis loop curves measured at the iron (red) and cobalt (green) edges essentially coincided after normalization,

further confirming that iron and cobalt are ferromagnetically coupled. Additionally, the square magnetic hysteresis loops at 80 K confirm that the easy magnetization direction of the FCGT nanoflakes is along the *c* axis. (see Figure S7, Supporting Information) Based on sum rules,[31] the spin (m_{spin}) and orbital moment ($m_{orbital}$) were calculated. The m_{spin} = 0.47 μB/Fe and $m_{orbital}$ = -0.02 μB/Fe and the m_{spin} = 0.39 μB/Co and $m_{orbital}$ = -0.05 μB/Co; thus, the estimated total moment m_{total} 0.79 μB/(Fe/Co) at room temperature, which is consistent with macroscopic magnetometry measurements.

3. Current-induced magnetization switching

Such a new phase of the FCGT system (i.e., a room-temperature layered magnet with broken inversion symmetry and perpendicular magnetization) suggests that it may be possible to realize current-induced magnetization switching by bulk SOT. The current-induced spin polarization vector (σ) can be written as $\sigma = \chi J$, where χ is the three-dimensional magnetoelectric pseudo-tensor, and J is the current. According to the point group C_{6v} (6mm) of FCGT, the magnetoelectric tensor can be expressed as:[32,33]

$$\chi = \begin{pmatrix} 0 & \chi_{xy} & 0 \\ \chi_{yx} & 0 & 0 \\ 0 & 0 & 0 \end{pmatrix},$$

and when a charge current is applied along the *x*-axis,

$$J = \begin{pmatrix} J_x \\ 0 \\ 0 \end{pmatrix},$$

then, the spin polarization is,

$$\sigma = \chi J = \begin{pmatrix} 0 & \chi_{xy} & 0 \\ \chi_{yx} & 0 & 0 \\ 0 & 0 & 0 \end{pmatrix} \begin{pmatrix} J_x \\ 0 \\ 0 \end{pmatrix} = \begin{pmatrix} 0 \\ \sigma_{yx} \\ 0 \end{pmatrix}$$

Since χ_{xy} and χ_{yx} are non-zero, *y*-axis spin polarization is generated when a current is applied along the *x*-axis. This mechanism is expected to lead to an antidamping torque [$\tau_{AD}\ \hat{m} \times (\hat{y} \times \hat{m})$] acting on the magnetization of the nanoflakes. Thus, R_{xy} as a function of a pulse current J_{pulse} was measured at room temperature in FCGT nanoflakes (as shown schematically in Figure 2**a**). The current pulse was applied along the *x* direction, and the time duration of the pulse current was 100 ms. To mitigate the effects of Joule heating, the ΔR_{xy} was taken after pulsing for 5 s. Due to the lack of lateral symmetry breaking in the crystal to generate an out-of-plane antidamping torque, a small in-plane external magnetic field along with the current direction was needed to deterministically switch the magnetization.

ΔR_{xy}-J_{pulse} loops at room temperature under an in-plane magnetic field H_x = ± 300 Oe (Figure 2**b**) reveal that ΔR_{xy} is switched from negative(positive) to positive(negative) at around J_{pulse} = −15 mA (+15 mA) under H_x = 300 Oe; strongly suggesting current-induced magnetization reversal. The chirality of the switching loops is reversed upon the reversal of the in-plane magnetic field direction, verifying that the perpendicular magnetization is indeed switched by the current-induced SOT. There is no change of ΔR_{xy} under zero magnetic field (see Figure S8, Supporting Information). The SOT switching occurs via a process of domain nucleation and subsequent domain-wall motion. The switching current density is ~7×10^6 A/cm^2 larger than the critical current density of the skyrmion motion (~ 1×10^6 A/cm^2; see Figure S2, Supporting Information), which is consistent with observations in multilayer thin-film systems.[34] In this measurement, the maximum value of ΔR_{xy} is ~ 0.1 **Ω**, which is ~ 22% of a complete magnetization reversal. The Joule heating induced by an applied pulse current would give a reduced magnetization and perpendicular magnetic anisotropy (see Figure S9-10, Supporting Information), leading to partial SOT switching, which is also observed in other systems.[10,35,36] Finally, a repeatable switching of the magnetization direction by current pulses is demonstrated at room temperature, wherein magnetization switching by current injection of ±18 mA under different external in-plane magnetic fields is realized (Figure 2**c**). The switching occurs once a small magnetic field is applied, and as the magnetic field increases, the ΔR_{xy} increases. The magnetization switching polarity reverses upon inverting the magnetic field polarity. All these observations are consistent with the features of SOT-induced magnetization switching. No current-induced magnetization switching loop is observed when the external in-plane magnetic field is applied along the *y* direction. (see Figure S11, Supporting Information)The anomalous Hall curves measured by magnetic field along the *x* and *y* directions nearly overlap, suggesting no in-plane magnetic anisotropy. (see Figure S12, Supporting Information) From these experiments, it can be concluded that the magnetization switching is caused by an antidamping-like torque; conversely, the field-like SOT is not responsible for magnetization switching.

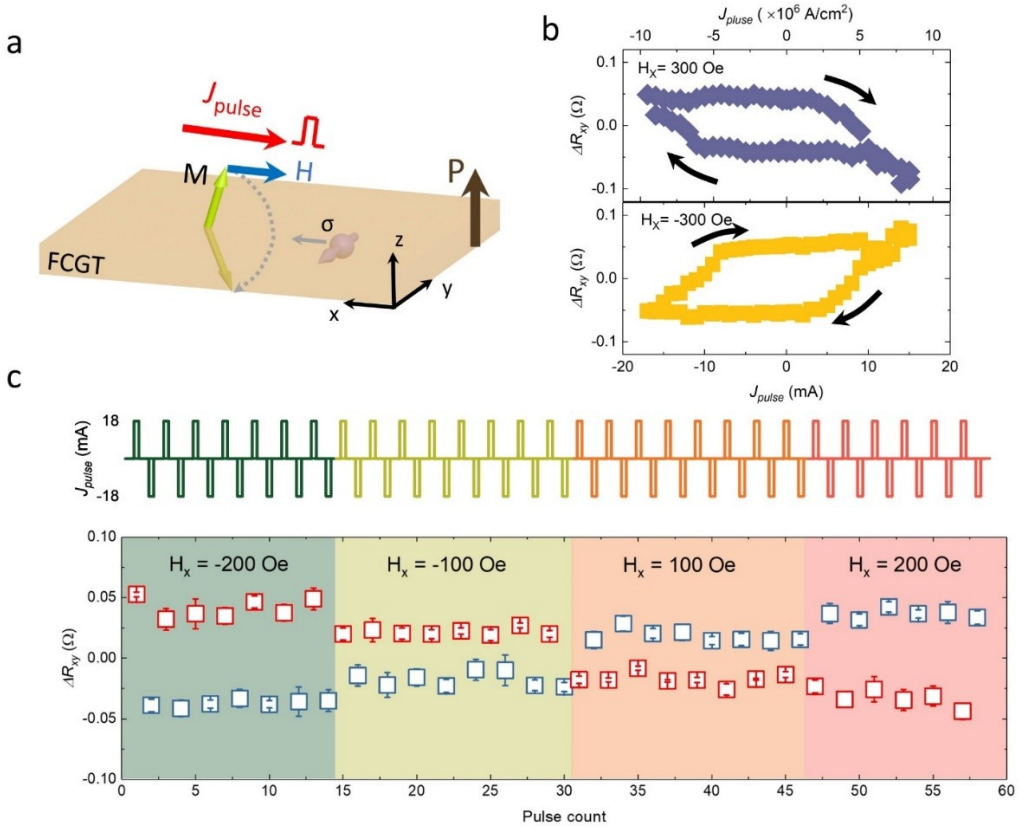

Figure 2. Room-temperature current-induced reversible magnetization switching. a) Schematic illustration of magnetization switching in FCGT. The magnetization in the FCGT flake is reversed by a pulse current along the *x*-direction under an in-plane external magnetic field parallel to the pulse current via the antidamping-like SOT. The magnetization is probed by the anomalous Hall resistance. **b**) Magnetization switching with current pulses under in-plane external magnetic fields $H_x = +300$ Oe (blue) and −300 Oe (yellow) at room temperature. **c**) Repeated, deterministic magnetization switching under J_{pulse} = ±18 mA at different magnetic fields. The up panel shows the pulse sequence, while the low panel shows the corresponding Hall resistances.

4. Current-induced effective field

In order to investigate the current-induced effective field, second harmonic Hall measurements were carried out at room temperature (a schematic of which is provided. Figure 3**a**). An *a.c.* current $I = I_0\sin(wt)$ was applied along the *x* direction at frequency = 23 Hz. When the in-plane external magnetic field exceeds the in-plane anisotropy field (H_k), a SOT-induced alternating, effective field causes the oscillation of the magnetization, which contributes to the second-harmonic Hall resistance ($R_{xy}^{2\omega}$). The magnetic field dependence of $R_{xy}^{2\omega}$ can be written as[37]:

$$R_{xy}^{2\omega} = \frac{R_{AHE}}{2}\frac{H_{eff}}{|H_x| - H_k} + R_{Thermal}\frac{H_x}{|H_x|},$$

, where R_{AHE} is the anomalous Hall resistance, H_{eff} is the effective field, $R_{Thermal}$ is the thermal contribution from anomalous Nernst and spin Seebeck effects, and H_k is obtained by fitting the 1ω signal in the low magnetic field region (from Figure 2**a**). The second harmonic Hall signals as a function of the magnetic field at a current density of 1.4 $\times 10^6$ A/cm^2 (Figure 3**b**) were obtained and, by fitting the 2ω signal, an effective SOT field was obtained. The J-dependent effective field H_{DL}, exhibiting a linear correlation, is also provided (Figure 3**c**). The slope is ~ 1.4×10^{-5} Oe cm^2/A for the FCGT system. The charge-to-spin conversion efficiency is estimated using the formula $q_{CS} = 2e\mu_0 M_s H_{DL}/\hbar J$, where M_s is the saturation magnetization of the FCGT, and $\hbar$ is the Planck constant. We calculated the q_{CS} = 0.13 nm^{-1} at room temperature, which is close to that of tantalum metal[38].

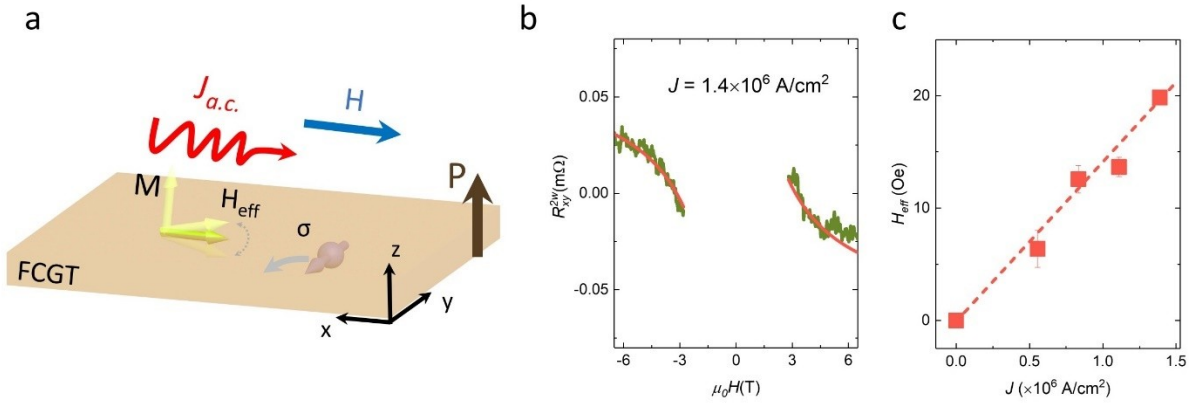

Figure 3 **Effective field measured by second harmonic Hall measurements at room temperature. a**) The schematic illustration of the spin-orbit effective fields in the FCGT nanoflake. **b**) A typical magnetic field dependence of second harmonic Hall resistance under a current J = 1.4×10^6 A/cm^2 at room temperature. **c**) Current-dependent effective field at room temperature.

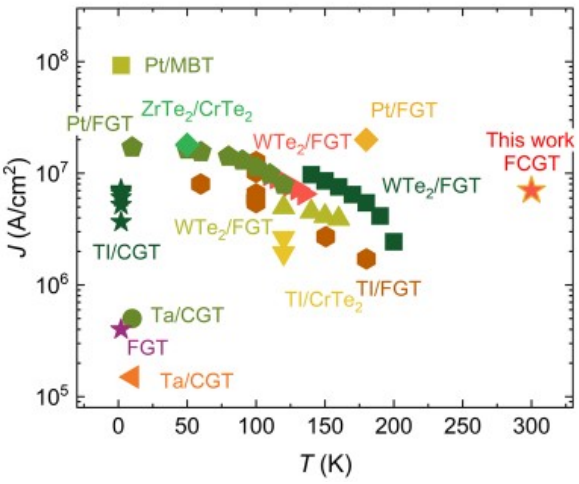

Figure 4 Current-induced magnetization switching of previously reported layered magnetic heterostructures. Magnetic heterostructures based on a topological insulator (TI) are more efficient than those comprised of Pt and/or semi-metal WTe_2. This work demonstrates a room-temperature, current-induced magnetization with a current density of ~ 10^6 A/cm^2 in the FCGT system. The reported data were taken from references, Pt/Fe_3GeT_2 (FGT)[35,39], WTe_2/FGT[2,40,41], TI/ FGT[42], FGT[19], Ta/$Cr_2Ge_2Te_6$ (CGT)[43,44], TI/CGT[45], TI/$CrTe_2$[46], $ZrTe_2$/$CrTe_2$[47], and Pt/$MnBi_2Te_4$(MBT)[48].

5. Conclusion

SOT-based magnetic tunnel junctions can realize low-power information storage, which is a promising way to the next generation of non-volatile magnetic random-access memories. As the feature size of magnetic tunnel junctions continues to decrease to satisfy ever-growing storage data density, current technologies based on traditional materials will reach their limit. [49,50] For this reason, the development and performances of 2D spintronic devices may be potentially important, providing a pathway to solving various technological issues. However, 2D magnets with perpendicular magnetic anisotropy tend to exhibit a low Curie temperature which means that the working temperature of 2D SOT devices has typically been < 200 K (Figure 4). The threshold current density of the magnetization switching of the layered magnet is 10^6 ~ 10^7 A/cm^2. Here, we report the observation of current-induced perpendicular magnetization self-switching in the FCGT layered ferromagnet at room temperature with a switching current in the range of 10^6 A/cm^2. Unlike most SOT devices, a spin-orbit coupling layer is not required in this device since the SOT is generated by the low symmetry within the bulk magnetic material itself. The magnetization direction can be repeatedly controlled by pulse current injection at room temperature. Recently, wafer-scale production of FGT thin

films via molecular-beam epitaxy has been achieved, and the resultant films exhibit high Curie temperatures.[51,52] In addition, a large tunneling magnetoresistance in Fe_3GeTe_2-based heterostructures has been realized.[53,54] Furthermore, a topological insulator layer as an extra spin current source of the bottom layer may help further reduce the critical switching current density.[37,55] Therefore, the FCGT system exhibits a promising application in 2D SOT-magnetic tunnel junctions, which can lead to the development of next-generation magnetic random access memories.[49,56-58]

6. Experimental Section/Methods

Sample preparation: High-quality FCGT single crystals were synthesized by the chemical vapor transfer method. FCGT flakes and h-BN capping layers were cleaved from tapes and transferred in sequence onto the center of four metal electrodes via a dry transfer method with PDMS stamp for electrical measurements. For XMCD measurement, FCGT flakes were transferred onto Norcada 30mm×30mm SiNx membrane window TEM grids, which consist of a 200 nm-thick membrane supported by a 200mm-thick hollow Si frame. The flakes used for XMCD measurements were larger than 30 mm×30 mm, so that all the detected X-rays were transmitted through the flakes, giving a maximum signal-to-noise ratio.

Scanning transmission electron microscopy (STEM): The cross-sectional STEM specimen was prepared using a Thermo Fisher Scientific Helios focused ion beam (FIB) with a final polishing step at 2 keV to minimize damage. HAADF-STEM image was recorded using a Cs-corrected Thermo Fisher Scientific "Kraken" Spectra 300 operated at 120 keV, with beam semi-convergence angle of 30 mrad and current of 30 pA. The image was applied with a Gaussian filter of 2 pixels to reduce high-frequency noise.

X-ray absorption spectroscopy (XAS) and X-ray magnetic circular dichroism (XMCD): The XAS and XMCD measurements were performed on Beamline 4.0.2 and 6.3.1 of the Advanced Light Source by switching the magnetization parallel and antiparallel to the propagation direction of 75% circularly polarized x-rays at normal incidence. XAS measurements with bulk-sensitive luminescence yield were carried out at 80 K and 300 K. By flipping the X-ray helicity at the fixed magnetic field of 1 T, we obtained the XMCD by taking the difference of XAS, μ^+-μ^-.

The XMCD spectra have been analyzed for both Fe and Co L edge according to the sum rules. The spin moment (m_{spin}) and orbital moment (m_{orbit}) can be calculated by the sum rule:[31]

$$m_{spin} = -6 \int_{L_3} ¿¿¿$$

$$m_{orbit} = -4 \int_{(L¿¿3+L_2)¿} ¿¿¿$$

where n_{3d} is 6.61 for the Fe element and 7.51 for the Co element.

Electrical transport measurements: In current-induced magnetization switching measurements, a Keithley 6221 source meter is used to apply a pulse current with a duration of 100 ms. After 5 s, the Hall resistance was recorded using a small *d.c*. excitation current (10 μA). Before conducting the magnetization switching experiment in Fig.2, we performed an initial pulse current process to establish a stable magnetic state.[35] For the harmonic Hall measurement, an *a.c.* current was applied by a Keithley 6221 current source. The frequency is fixed at 23 Hz. The harmonic voltages were measured by SR 830 lock-in preamplifiers.

Supporting Information

Supporting Information is available from the Wiley Online Library or from the author.

Acknowledgments

H.R.Z., X.C, and T.Y.W. contributed equally to this work. Work at Lawrence Berkeley National Laboratory was primarily supported by the U.S. Department of Energy, Office of Science, Office of Basic Energy Sciences, Materials Sciences and Engineering Division under Contract No. DE-AC02-05CH11231 within the Quantum Materials Program (No. KC2202) and U.S. Department of Energy, Office of Science, Office of Basic Energy Sciences, Materials Sciences and Engineering Division under Contract No. DE-AC02-05-CH11231 (Codesign of Ultra-Low-Voltage Beyond CMOS Microelectronics) for the development of materials for low-power microelectronics. Y.T.S., and D.A.M. acknowledge financial support from the Department of Defense, Air Force Office of Scientific Research under Grant No. FA9550-18-1-0480. Z. Q. and T. W. acknowledge the US Department of Energy, Office of Science, Office of Basic Energy Sciences, Materials Sciences and Engineering Division under Contract No. DE-AC02-05CH11231 (van der Waals heterostructures program, KCWF16). X.H. is supported by the SRC-ASCENT center, which is part of the SRC-JUMP program. F.M. and J.Y. acknowledge the support by Intel Corporation under a grant titled Valleytronics Center. H.P. acknowledges support from the Army Research Laboratory via the Collaborative for Hierarchical Agile and Responsive Materials (CHARM) under cooperative agreement W911NF-19-2-0119. P.M. and R.R. acknowledge funding from the Department of Defense, ARO Grant No. W911NF-21-2-0162 (ETHOS). The devices for transport measurements were fabricated in the UC Berkeley Marvell Nanofabrication Laboratory.

Received: ((will be filled in by the editorial staff))

Revised: ((will be filled in by the editorial staff))

Published online: ((will be filled in by the editorial staff))

Reference:

[1] D. MacNeill, G. M. Stiehl, M. H. D. Guimaraes, R. A. Buhrman, J. Park, and D. C. Ralph, Control of spin–orbit torques through crystal symmetry in WTe_2/ferromagnet bilayers Nature Phys. **13**, 300 (2017).

[2] I. H. Kao, R. Muzzio, H. Zhang, M. Zhu, J. Gobbo, S. Yuan, D. Weber, R. Rao, J. Li, J. H. Edgar, J. E. Goldberger, J. Yan, D. G. Mandrus, J. Hwang, R. Cheng, J. Katoch, and S. Singh, Deterministic switching of a perpendicularly polarized magnet using unconventional spin–orbit torques in WTe_2 Nat. Mater. (2022).

[3] S. Shi, S. Liang, Z. Zhu, K. Cai, S. D. Pollard, Y. Wang, J. Wang, Q. Wang, P. He, J. Yu, G. Eda, G. Liang, and H. Yang, All-electric magnetization switching and Dzyaloshinskii–Moriya interaction in WTe_2/ferromagnet heterostructures Nat. Nanotech. **14**, 945 (2019).

[4] L. Liu, C. Zhou, X. Shu, C. Li, T. Zhao, W. Lin, J. Deng, Q. Xie, S. Chen, J. Zhou, R. Guo, H. Wang, J. Yu, S. Shi, P. Yang, S. Pennycook, A. Manchon, and J. Chen, Symmetry-dependent field-free switching of perpendicular magnetization Nat. Nanotech. **16**, 277 (2021).

[5] X. Chen, S. Shi, G. Shi, X. Fan, C. Song, X. Zhou, H. Bai, L. Liao, Y. Zhou, H. Zhang, A. Li, Y. Chen, X. Han, S. Jiang, Z. Zhu, H. Wu, X. Wang, D. Xue, H. Yang, and F. Pan, Observation of the antiferromagnetic spin Hall effect Nat. Mater. **20**, 800 (2021).

[6] T. Nan, C. X. Quintela, J. Irwin, G. Gurung, D. F. Shao, J. Gibbons, N. Campbell, K. Song, S. Y. Choi, L. Guo, R. D. Johnson, P. Manuel, R. V. Chopdekar, I. Hallsteinsen, T. Tybell, P. J. Ryan, J. W. Kim, Y. Choi, P. G. Radaelli, D. C. Ralph, E. Y. Tsymbal, M. S. Rzchowski, and C. B. Eom, Controlling spin current polarization through non-collinear antiferromagnetism Nat. Commun. **11**, 4671 (2020).

[7] H. Bai, L. Han, X. Y. Feng, Y. J. Zhou, R. X. Su, Q. Wang, L. Y. Liao, W. X. Zhu, X. Z. Chen, F. Pan, X. L. Fan, and C. Song, Observation of Spin Splitting Torque in a Collinear Antiferromagnet RuO_2 Phys. Rev. Lett. **128**, 197202 (2022).

[8] A. Bose, N. J. Schreiber, R. Jain, D.-F. Shao, H. P. Nair, J. Sun, X. S. Zhang, D. A. Muller, E. Y. Tsymbal, D. G. Schlom, and D. C. Ralph, Tilted spin current generated by the collinear antiferromagnet ruthenium dioxide Nat. Electron. **5**, 267 (2022).

[9] A. Chernyshov, M. Overby, X. Liu, J. K. Furdyna, Y. Lyanda-Geller, and L. P. Rokhinson, Evidence for reversible control of magnetization in a ferromagnetic material by means of spin–orbit magnetic field Nature Phys. **5**, 656 (2009).

[10] R. Yoshimi, K. Yasuda, A. Tsukazaki, K. S. Takahashi, M. Kawasaki, and Y. Tokura, Current-driven magnetization switching in ferromagnetic bulk Rashba semiconductor (Ge,Mn)Te Sci. Adv. **4**, eaat9989 (2018).

[11] M. Tang, K. Shen, S. Xu, H. Yang, S. Hu, W. Lü, C. Li, M. Li, Z. Yuan, S. J. Pennycook, K. Xia, A. Manchon, S. Zhou, and X. Qiu, Bulk Spin Torque-Driven Perpendicular Magnetization Switching in $L1_0$ FePt Single Layer Adv. Mater. **32**, 2002607 (2020).

[12] R. Q. Zhang, L. Y. Liao, X. Z. Chen, T. Xu, L. Cai, M. H. Guo, H. Bai, L. Sun, F. H. Xue, J. Su, X. Wang, C. H. Wan, H. Bai, Y. X. Song, R. Y. Chen, N. Chen, W. J. Jiang, X. F. Kou, J. W. Cai, H. Q. Wu, F. Pan, and C. Song, Current-induced magnetization switching in a CoTb amorphous single layer Phys. Rev. B **101**, 214418 (2020).

[13] Z. Zheng, Y. Zhang, V. Lopez-Dominguez, L. Sánchez-Tejerina, J. Shi, X. Feng, L. Chen, Z. Wang, Z. Zhang, K. Zhang, B. Hong, Y. Xu, Y. Zhang, M. Carpentieri, A. Fert, G. Finocchio, W. Zhao, and P. Khalili Amiri, Field-free spin-orbit torque-induced switching of perpendicular magnetization in a ferrimagnetic layer with a vertical composition gradient Nat. Commun. **12**, 4555 (2021).

[14] Q. Liu, L. Zhu, X. S. Zhang, D. A. Muller, and D. C. Ralph, Giant bulk spin–orbit torque and efficient electrical switching in single ferrimagnetic FeTb layers with strong perpendicular magnetic anisotropy Applied Physics Reviews **9**, 021402 (2022).
[15] L. Liu, C. Zhou, T. Zhao, B. Yao, J. Zhou, X. Shu, S. Chen, S. Shi, S. Xi, D. Lan, W. Lin, Q. Xie, L. Ren, Z. Luo, C. Sun, P. Yang, E.-J. Guo, Z. Dong, A. Manchon, and J. Chen, Current-induced self-switching of perpendicular magnetization in CoPt single layer Nat. Commun. **13**, 3539 (2022).
[16] H. Kurebayashi, J. H. Garcia, S. Khan, J. Sinova, and S. Roche, Magnetism, symmetry and spin transport in van der Waals layered systems Nat. Rev. Phys. **4**, 150 (2022).
[17] N. L. Nair, E. Maniv, C. John, S. Doyle, J. Orenstein, and J. G. Analytis, Electrical switching in a magnetically intercalated transition metal dichalcogenide Nat. Mater. **19**, 153 (2020).
[18] K. Zhang, S. Han, Y. Lee, M. J. Coak, J. Kim, I. Hwang, S. Son, J. Shin, M. Lim, D. Jo, K. Kim, D. Kim, H.-W. Lee, and J.-G. Park, Gigantic Current Control of Coercive Field and Magnetic Memory Based on Nanometer-Thin Ferromagnetic van der Waals Fe_3GeTe_2 Adv. Mater. **33**, 2004110 (2021).
[19] K. Zhang, Y. Lee, M. J. Coak, J. Kim, S. Son, I. Hwang, D.-S. Ko, Y. Oh, I. Jeon, D. Kim, C. Zeng, H.-W. Lee, and J.-G. Park, Highly Efficient Nonvolatile Magnetization Switching and Multi-Level States by Current in Single Van der Waals Topological Ferromagnet Fe_3GeTe_2 Adv. Fun. Mater. **31**, 2105992 (2021).
[20] F. Martin, K. Lee, M. Schmitt, A. Liedtke, A. Shahee, H. T. Simensen, T. Scholz, T. G. Saunderson, D. Go, M. Gradhand, Y. Mokrousov, T. Denneulin, A. Kovács, B. Lotsch, A. Brataas, and M. Kläui, Strong bulk spin–orbit torques quantified in the van der Waals ferromagnet Fe_3GeTe_2 Mater. Res. Lett. **11**, 84 (2023).
[21] A. Chakraborty, A. K. Srivastava, A. K. Sharma, A. K. Gopi, K. Mohseni, A. Ernst, H. Deniz, B. K. Hazra, S. Das, P. Sessi, I. Kostanovskiy, T. Ma, H. L. Meyerheim, and S. S. P. Parkin, Magnetic Skyrmions in a Thickness Tunable 2D Ferromagnet from a Defect Driven Dzyaloshinskii–Moriya Interaction Adv. Mater. **34**, 2108637 (2022).
[22] J. Seo, D. Y. Kim, E. S. An, K. Kim, G.-Y. Kim, S.-Y. Hwang, D. W. Kim, B. G. Jang, H. Kim, G. Eom, S. Y. Seo, R. Stania, M. Muntwiler, J. Lee, K. Watanabe, T. Taniguchi, Y. J. Jo, J. Lee, B. I. Min, M. H. Jo, H. W. Yeom, S.-Y. Choi, J. H. Shim, and J. S. Kim, Nearly room temperature ferromagnetism in a magnetic metal-rich van der Waals metal Sci. Adv. **6**, eaay8912 (2020).
[23] A. F. May, D. Ovchinnikov, Q. Zheng, R. Hermann, S. Calder, B. Huang, Z. Fei, Y. Liu, X. Xu, and M. A. McGuire, Ferromagnetism Near Room Temperature in the Cleavable van der Waals Crystal Fe_5GeTe_2 ACS Nano **13**, 4436 (2019).
[24] Z. Li, M. Tang, J. Huang, F. Qin, L. Ao, Z. Shen, C. Zhang, P. Chen, X. Bi, C. Qiu, Z. Yu, K. Zhai, T. Ideue, L. Wang, Z. Liu, Y. Tian, Y. Iwasa, and H. Yuan, Magnetic Anisotropy Control with Curie Temperature above 400 K in a van der Waals Ferromagnet for Spintronic Device Adv. Mater. **34**, 2201209 (2022).
[25] H. Zhang, Y.-T. Shao, R. Chen, X. Chen, S. Susarla, D. Raftrey, J. T. Reichanadter, L. Caretta, X. Huang, N. S. Settineri, Z. Chen, J. Zhou, E. Bourret-Courchesne, P. Ercius, J. Yao, P. Fischer, J. B. Neaton, D. A. Muller, R. J. Birgeneau, and R. Ramesh, A room temperature polar magnetic metal Phys. Rev. Mater. **6**, 044403 (2022).
[26] X. Chen, Y.-T. Shao, R. Chen, S. Susarla, T. Hogan, Y. He, H. Zhang, S. Wang, J. Yao, P. Ercius, D. A. Muller, R. Ramesh, and R. J. Birgeneau, Pervasive beyond Room-Temperature Ferromagnetism in a Doped van der Waals Magnet Phys. Rev. Lett. **128**, 217203 (2022).
[27] X. Chen, E. Schierle, Y. He, M. Vranas, J. W. Freeland, J. L. McChesney, R. Ramesh, R. J. Birgeneau, and A. Frano, Antiferromagnetic order in Co-doped Fe_5GeTe_2 probed by resonant magnetic x-ray scattering Phys. Rev. Mater. **6**, 094404 (2022).
[28] X. Chen, W. Tian, Y. He, H. Zhang, T. L. Werner, S. Lapidus, J. P. C. Ruff, R. Ramesh, and R. J. Birgeneau, Thermal cycling induced alteration of the stacking order and spin-flip in the room temperature van der Waals magnet Fe_5GeTe_2 arXiv:2209.04560 (2022).
[29] H. Wu, L. Chen, P. Malinowski, J.-w. Huang, Q. Deng, K. Scott, B. G. Jang, J. P. C. Ruff, Y. He, X. Chen, C. Hu, Z. Yue, J. S. Oh, X. Teng, Y. Guo, M. Klemm, C. Shi, Y.-S. Shi, C. S. G. K. Setty, T. L. Werner, M. Hashimoto, D. Lu, T. Yilmaz, E. Vescovo, S. K. Mo, A. V. Fedorov, J. D.

Denlinger, Y.-p. Xie, B. Gao, J. Kono, P. Dai, Y. Han, X. Xu, R. J. Birgeneau, J.-X. Zhu, E. H. d. S. Neto, L. Wu, J. H. Chu, Q. Si, and M. Yi, (arXiv:2307.03154, 2023).
[30] I. Lemesh, K. Litzius, M. Böttcher, P. Bassirian, N. Kerber, D. Heinze, J. Zázvorka, F. Büttner, L. Caretta, M. Mann, M. Weigand, S. Finizio, J. Raabe, M.-Y. Im, H. Stoll, G. Schütz, B. Dupé, M. Kläui, and G. S. D. Beach, Current-Induced Skyrmion Generation through Morphological Thermal Transitions in Chiral Ferromagnetic Heterostructures Adv. Mater. **30**, 1805461 (2018).
[31] C. T. Chen, Y. U. Idzerda, H. J. Lin, N. V. Smith, G. Meigs, E. Chaban, G. H. Ho, E. Pellegrin, and F. Sette, Experimental Confirmation of the X-Ray Magnetic Circular Dichroism Sum Rules for Iron and Cobalt Phys. Rev. Lett. **75**, 152 (1995).
[32] C. Ciccarelli, L. Anderson, V. Tshitoyan, A. J. Ferguson, F. Gerhard, C. Gould, L. W. Molenkamp, J. Gayles, J. Železný, L. Šmejkal, Z. Yuan, J. Sinova, F. Freimuth, and T. Jungwirth, Room-temperature spin–orbit torque in NiMnSb Nature Phys. **12**, 855 (2016).
[33] A. Manchon, J. Železný, I. M. Miron, T. Jungwirth, J. Sinova, A. Thiaville, K. Garello, and P. Gambardella, Current-induced spin-orbit torques in ferromagnetic and antiferromagnetic systems Rev. Mod. Phys. **91**, 035004 (2019).
[34] S. Emori, U. Bauer, S.-M. Ahn, E. Martinez, and G. S. D. Beach, Current-driven dynamics of chiral ferromagnetic domain walls Nat. Mater. **12**, 611 (2013).
[35] X. Wang, J. Tang, X. Xia, C. He, J. Zhang, Y. Liu, C. Wan, C. Fang, C. Guo, W. Yang, Y. Guang, X. Zhang, H. Xu, J. Wei, M. Liao, X. Lu, J. Feng, X. Li, Y. Peng, H. Wei, R. Yang, D. Shi, X. Zhang, Z. Han, Z. Zhang, G. Zhang, G. Yu, and X. Han, Current-driven magnetization switching in a van der Waals ferromagnet Fe_3GeTe_2 Sci. Adv. **5**, eaaw8904 (2019).
[36] L. Liu, Q. Qin, W. Lin, C. Li, Q. Xie, S. He, X. Shu, C. Zhou, Z. Lim, J. Yu, W. Lu, M. Li, X. Yan, S. J. Pennycook, and J. Chen, Current-induced magnetization switching in all-oxide heterostructures Nat. Nanotech. **14**, 939 (2019).
[37] Y. Fan, P. Upadhyaya, X. Kou, M. Lang, S. Takei, Z. Wang, J. Tang, L. He, L.-T. Chang, M. Montazeri, G. Yu, W. Jiang, T. Nie, R. N. Schwartz, Y. Tserkovnyak, and K. L. Wang, Magnetization switching through giant spin–orbit torque in a magnetically doped topological insulator heterostructure Nat. Mater. **13**, 699 (2014).
[38] H. Wu, P. Zhang, P. Deng, Q. Lan, Q. Pan, S. A. Razavi, X. Che, L. Huang, B. Dai, K. Wong, X. Han, and K. L. Wang, Room-Temperature Spin-Orbit Torque from Topological Surface States Phys. Rev. Lett. **123**, 207205 (2019).
[39] M. Alghamdi, M. Lohmann, J. Li, P. R. Jothi, Q. Shao, M. Aldosary, T. Su, B. P. T. Fokwa, and J. Shi, Highly Efficient Spin–Orbit Torque and Switching of Layered Ferromagnet Fe_3GeTe_2 Nano Lett. **19**, 4400 (2019).
[40] I. Shin, W. J. Cho, E.-S. An, S. Park, H.-W. Jeong, S. Jang, W. J. Baek, S. Y. Park, D.-H. Yang, J. H. Seo, G.-Y. Kim, M. N. Ali, S.-Y. Choi, H.-W. Lee, J. S. Kim, S. D. Kim, and G.-H. Lee, Spin–Orbit Torque Switching in an All-Van der Waals Heterostructure Adv. Mater. **34**, 2101730 (2022).
[41] X.-G. Ye, P.-F. Zhu, W.-Z. Xu, N. Shang, K. Liu, and Z.-M. Liao, Orbit-Transfer Torque Driven Field-Free Switching of Perpendicular Magnetization Chin. Phys. Lett. **39**, 037303 (2022).
[42] R. Fujimura, R. Yoshimi, M. Mogi, A. Tsukazaki, M. Kawamura, K. S. Takahashi, M. Kawasaki, and Y. Tokura, Current-induced magnetization switching at charge-transferred interface between topological insulator (Bi,Sb)2Te_3 and van der Waals ferromagnet Fe_3GeTe_2 App. Phys. Lett. **119**, 032402 (2021).
[43] V. Ostwal, T. Shen, and J. Appenzeller, Efficient Spin-Orbit Torque Switching of the Semiconducting Van Der Waals Ferromagnet $Cr_2Ge_2Te_6$ Adv. Mater. **32**, 1906021 (2020).
[44] V. Gupta, T. M. Cham, G. M. Stiehl, A. Bose, J. A. Mittelstaedt, K. Kang, S. Jiang, K. F. Mak, J. Shan, R. A. Buhrman, and D. C. Ralph, Manipulation of the van der Waals Magnet $Cr_2Ge_2Te_6$ by Spin–Orbit Torques Nano Lett. **20**, 7482 (2020).
[45] M. Mogi, K. Yasuda, R. Fujimura, R. Yoshimi, N. Ogawa, A. Tsukazaki, M. Kawamura, K. S. Takahashi, M. Kawasaki, and Y. Tokura, Current-induced switching of proximity-induced ferromagnetic surface states in a topological insulator Nat. Commun. **12**, 1404 (2021).

[46] X. Liu, Y. Xia, L. Gao, P. Huang, L. Liao, B. Cui, D. Backes, G. v. d. Laan, T. Hesjedal, Y. Ji, P. Chen, F. Wu, M. Wang, J. Zhang, G. Yu, C. Song, Y. Chen, Z. Liu, Y. Yang, Y. Peng, G. Li, Q. Yao, and X. Kou, Wafer-scale epitaxial growth of the thickness-controllable van der Waals ferromagnet $CrTe_2$ for reliable magnetic memory applications arXiv:2207.05944 (2022).
[47] Y. Ou, W. Yanez, R. Xiao, M. Stanley, S. Ghosh, B. Zheng, W. Jiang, Y.-S. Huang, T. Pillsbury, A. Richardella, C. Liu, T. Low, V. H. Crespi, K. A. Mkhoyan, and N. Samarth, $ZrTe_2/CrTe_2$: an epitaxial van der Waals platform for spintronics Nat. Commun. **13**, 2972 (2022).
[48] C. Ye, X. Xie, W. Lv, K. Huang, A. J. Yang, S. Jiang, X. Liu, D. Zhu, X. Qiu, M. Tong, T. Zhou, C.-H. Hsu, G. Chang, H. Lin, P. Li, K. Yang, Z. Wang, T. Jiang, and X. Renshaw Wang, Nonreciprocal Transport in a Bilayer of $MnBi_2Te_4$ and Pt Nano Lett. **22**, 1366 (2022).
[49] H. Yang, S. O. Valenzuela, M. Chshiev, S. Couet, B. Dieny, B. Dlubak, A. Fert, K. Garello, M. Jamet, D.-E. Jeong, K. Lee, T. Lee, M.-B. Martin, G. S. Kar, P. Sénéor, H.-J. Shin, and S. Roche, Two-dimensional materials prospects for non-volatile spintronic memories Nature **606**, 663 (2022).
[50] B. Dieny, I. L. Prejbeanu, K. Garello, P. Gambardella, P. Freitas, R. Lehndorff, W. Raberg, U. Ebels, S. O. Demokritov, J. Akerman, A. Deac, P. Pirro, C. Adelmann, A. Anane, A. V. Chumak, A. Hirohata, S. Mangin, S. O. Valenzuela, M. C. Onbaşlı, M. d'Aquino, G. Prenat, G. Finocchio, L. Lopez-Diaz, R. Chantrell, O. Chubykalo-Fesenko, and P. Bortolotti, Opportunities and challenges for spintronics in the microelectronics industry Nat. Electron. **3**, 446 (2020).
[51] S. Liu, X. Yuan, Y. Zou, Y. Sheng, C. Huang, E. Zhang, J. Ling, Y. Liu, W. Wang, C. Zhang, J. Zou, K. Wang, and F. Xiu, Wafer-scale two-dimensional ferromagnetic Fe_3GeTe_2 thin films grown by molecular beam epitaxy npj 2D Mater. Appl. **1**, 30 (2017).
[52] M. Ribeiro, G. Gentile, A. Marty, D. Dosenovic, H. Okuno, C. Vergnaud, J.-F. Jacquot, D. Jalabert, D. Longo, P. Ohresser, A. Hallal, M. Chshiev, O. Boulle, F. Bonell, and M. Jamet, Large-scale epitaxy of two-dimensional van der Waals room-temperature ferromagnet Fe_5GeTe_2 npj 2D Mater. Appl. **6**, 10 (2022).
[53] Z. Wang, D. Sapkota, T. Taniguchi, K. Watanabe, D. Mandrus, and A. F. Morpurgo, Tunneling Spin Valves Based on Fe_3GeTe_2/hBN/Fe_3GeTe_2 van der Waals Heterostructures Nano Lett. **18**, 4303 (2018).
[54] W. Zhu, H. Lin, F. Yan, C. Hu, Z. Wang, L. Zhao, Y. Deng, Z. R. Kudrynskyi, T. Zhou, Z. D. Kovalyuk, Y. Zheng, A. Patanè, I. Žutić, S. Li, H. Zheng, and K. Wang, Large Tunneling Magnetoresistance in van der Waals Ferromagnet/Semiconductor Heterojunctions Adv. Mater. **33**, 2104658 (2021).
[55] X. Chen, H. Bai, Y. Ji, Y. Zhou, L. Liao, Y. You, W. Zhu, Q. Wang, L. Han, X. Liu, A. Li, X. Han, J. Yin, X. Kou, F. Pan, and C. Song, Control of spin current and antiferromagnetic moments via topological surface state Nat. Electron. (2022).
[56] W. Han, Perspectives for spintronics in 2D materials APL Mater. **4**, 032401 (2016).
[57] X. Lin, W. Yang, K. L. Wang, and W. Zhao, Two-dimensional spintronics for low-power electronics Nat. Electron. **2**, 274 (2019).
[58] K. S. Burch, D. Mandrus, and J.-G. Park, Magnetism in two-dimensional van der Waals materials Nature **563**, 47 (2018).

ToC figure

A room-temperature current-induced magnetization self-switching was achieved in a van der Waals polar magnetic metal, $Fe_{2.5}Co_{2.5}GeTe_2$.

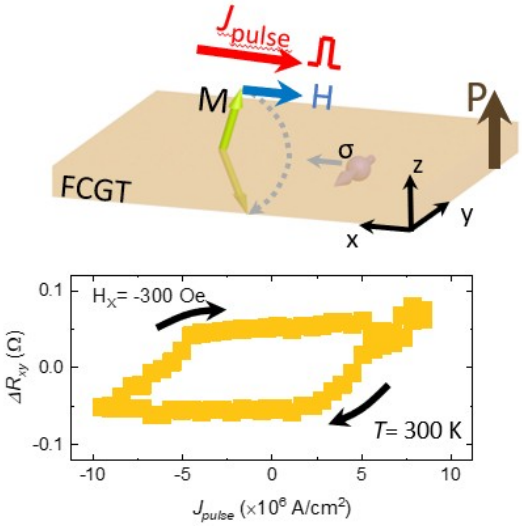

Supporting Information

Room-temperature, current-induced magnetization self-switching in a van der Waals ferromagnet

Hongrui Zhang[#,], Xiang Chen[#], Tianye Wang[#], Xiaoxi Huang, Xianzhe Chen, Yu-Tsun Shao, Fanhao Meng, Peter Meisenheimer, Alpha N'Diaye, Christoph Klewe, Padraic Shafer, Hao Pan, Yanli Jia, Michael F. Crommie, Lane W. Martin, Jie Yao, Ziqiang Qiu, David A. Muller, Robert J. Birgeneau, Ramamoorthy Ramesh[*]*

Email: hongruizhang@berkeley.edu, rramesh@berkeley.edu
[#]These authors contributed equally: Hongrui Zhang, Xiang Chen, Tianye Wang.

1. Crystal structure of FCGT

$(Fe_{0.5}, Co_{0.5})_5GeTe_2$ is a hexagonal wurtzite structure. The space group is $P6_3mc$ (No. 186); the point group is C_{6v} (6mm). The lattice parameters a = 4.01 Å, and c =19.43 Å. Figure S1 shows the side view (**a**) and top view (**b**) of the crystalline structure. The sublayers stacked AA'-type along the c-axis. There are six layers (Fe-Fe-Fe-Ge-Fe-Fe) in the middle of the Te layers, compared to seven layers (Fe-Fe-Fe-Ge-Fe-Fe-Fe) for the AA phase ($(Fe_{0.55}, Co_{0.45})_5GeTe_2$). [1] The Fe1 site is orderly occupied in the AA' phase, which induces a polar axis along the c axis of the crystal.

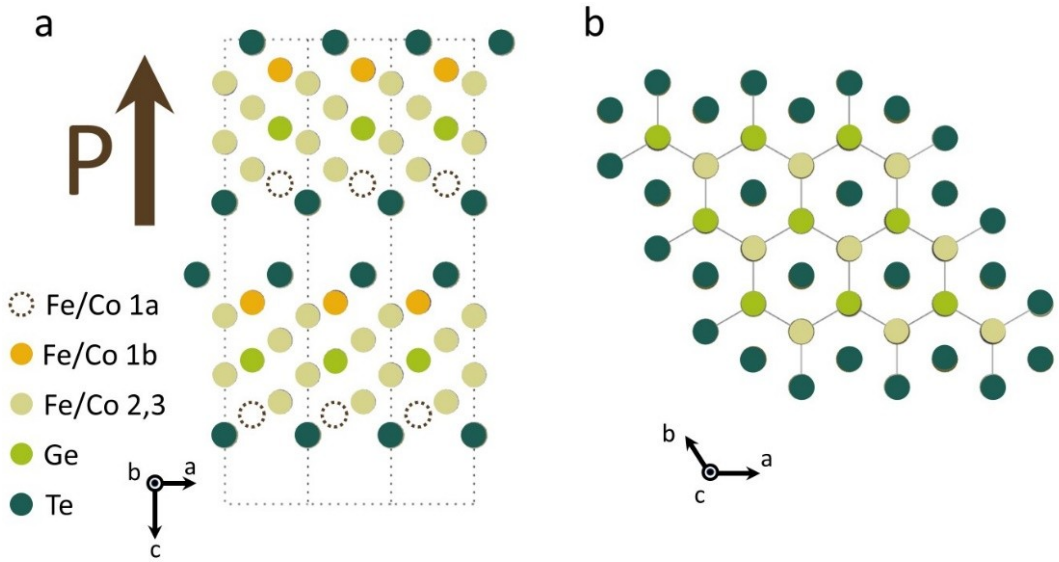

Figure S1 Schematic image of crystal structure. The crystal structure of FCGT, **a)** side view and **b)** top view.

2. Stabilization of skyrmion and current-induced skyrmion motion in a thick FCGT nanoflake

We exfoliated FCGT nanoflakes on the SiO_2/Si substrate, then immediately transferred the sample into the magnetron sputtering chamber and capped a 6-nm-thick Ti film on the top to avoid degradation. The thickness of the nanoflake is ~ 135 nm, measured by atomic force microscopy (AFM). The magnetic domain structure was obtained by magnetic force microscopy (MFM) at room temperature in Fig. S2**a**. A labyrinthine Néel-type domain was observed at zero magnetic field. The labyrinthine domain gradually breaks into skyrmions as the out-of-plane magnetic field increases. When the field reaches 110 mT, the skyrmion lattice is stabilized. Finally, it goes to a single domain under a 145 mT field.

The current-driven skyrmion motion can generate an emergent magnetoelectric field.[2] The skyrmions carry an emergent magnetic field, leading to the topological Hall effect. The emergent electric field can be generated perpendicular to the current direction and measured by the imaginary part of the odd harmonic Hall measurement.[3] Figure S2**b** shows the anomalous Hall curve at room temperature for a 136-nm-thick nanoflake hosting skyrmions. Compared to the square loop in the thin nanoflake, the curve shows sheared out-of-plane loops, indicating a multidomain state. In high-order harmonic Hall measurements, we input a sine-wave current ($□=□_0\sin□□$) and measure the imaginary components of the third harmonic voltage ($\Im R_{xy}^{3\omega}$). Figure S2**c** shows the magnetic field dependence of the imaginary part of the 3ω signal at different current densities. Only a background signal was observed under a current density of 0.79 MA/cm^2. Once J >1.27 MA/cm^2, two peaks near the skyrmion phase region emerge. In previous work [4], the skyrmion can be stabilized only at an annihilated state but at a nucleated state. However, we observe peaks in both states. This indicates that the current can induce skyrmion formation at the nucleated state, and its threshold value is almost identical to that of skyrmion motion at the annihilated state. The emergent electric field induced by skyrmion motion is generated perpendicular to the current direction. Thus, no voltage signal along the current direction was observed, as shown in Figure S2**d**. As the J increases, the intensity of the peaks also increases. The J-dependent intensity of peaks is summarized in Figure S2**e**, obtained the threshold J of skyrmion motion is ~ 1MA/cm^2. Figure S3**e** shows the frequency-dependent intensity of the peaks. We found that the intensity is almost the same as the frequency increases until f ~10^5 Hz, which means the skyrmion can move fast and follow the oscillation of the current.

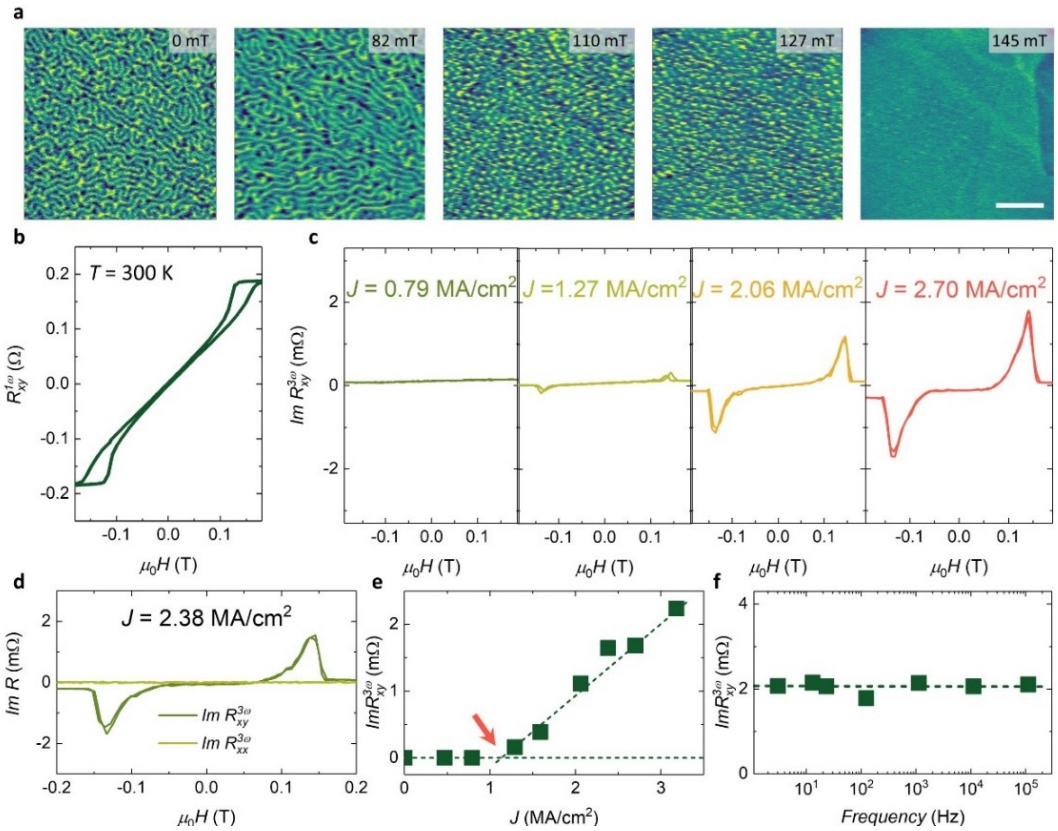

Figure S2 Stabilization of skyrmions and Current-induced skyrmions motion at room temperature. **a**) Magnetic field dependence of the MFM images captured at room temperature in a 135-nm-thick nanoflake. The scale bar is 2 μm. **b**) Anomalous Hall curve of a 136-nm-thick nanoflake at room temperature. **c**) Magnetic field dependence of the imaginary part of the 3ω signal ($\Im R_{xy}^{3\omega}$) measured with different current densities at room temperature. **d**) Magnetic field dependence of $\Im R_{xy}^{3\omega}$ and $\Im R_{xx}^{3\omega}$ measured with J = 2.38 MA/cm^2 at room temperature. **e**), **f)** Current density and frequency dependence of the $\Im R_{xy}^{3\omega}$ at room temperature.

3. Single domain thin FCGT nanoflakes and devices

Figure S3 displays the AFM and the corresponding MFM images for ~33 nm thick nanoflakes at room temperature. Compared to the stripe domain in the thick nanoflakes, the thin nanoflakes tend to host a larger-size domain or a single domain in Fig. S3**b**. The stabilization of a single domain at zero field is conducive to achieving magnetization switching. Then, we used similar thickness nanoflakes to make the magnetization switching devices, as shown in Fig. S4**a**. The nanoflake thickness is ~30 nm, determined by analyzing the AFM line profile.

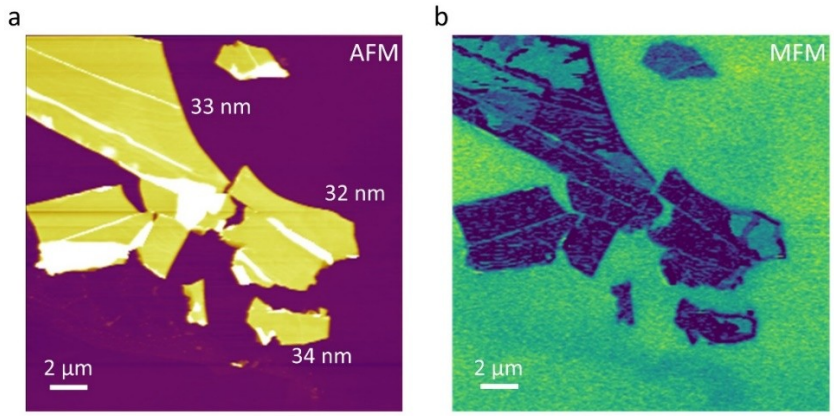

Figure S3 The magnetic domain patterns in thin nanoflakes. The FCGT nanoflakes on SiO_2/Si substrate are capped by 6-nm-thick Ti metal to avoid its degradation. **a**) The thickness of the nanoflakes in the AFM image is around 33 nm. **b**) The MFM image of as-grown nanoflakes is measured at room temperature.

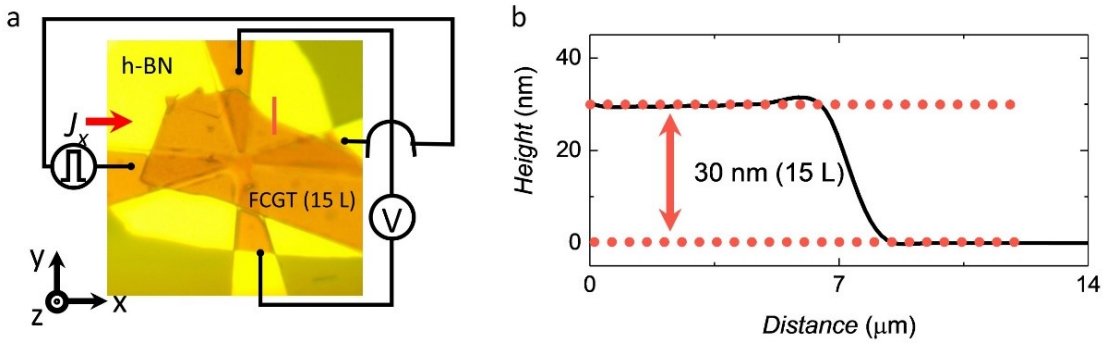

Figure S4 The thickness of the FCGT nanoflake in the device. a) The optical image of the device. The line profile of height along the red line in Fig. S4**a** was obtained by the AFM, as shown in Fig. S4**b**. The thickness of the FCGT nanoflake in this device is ~ 30 nm.

4. Raman measurement

The Raman spectra were measured using a Horiba Jobin Yvon LabRAM ARAMIS confocal Raman microscope. Linearly polarized laser excitation (λ =532 nm) with normal incidence was focused onto the sample through an objective lens (Olympus 100x, focal spot ~ 2 μm^2). Another polarizer was placed parallel to the excitation polarization before the detector, and the sample was rotated in-plane to measure the polarization-dependent Raman signal in the parallel configuration. The angle-dependent Raman pattern (Fig. S5) indicates no in-plane anisotropy within the FCGT flake.

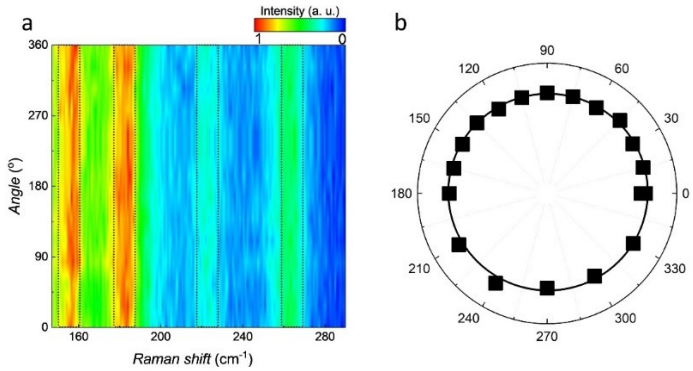

Figure S5 Raman measurements. a) A typical angle-dependent polarized Raman spectra of the FCGT flake in the parallel-polarized configuration by rotating the sample with respect to the excitation laser polarization direction. **b)** The representative angle-dependent Raman intensities at ~183 cm^{-1}. The intensity is almost the same, indicating no in-plane low symmetry.

5. XMCD measurements

The XAS/XMCD spectra were measured at 80 K under a magnetic field of 1.6 T in Fig. S6. The easy magnetization plane of pure Fe_5GeTe_2 and $Fe_{3.85}Co_{1.15}GeTe_2$ is in plane. The angle between the X-ray incidence direction and the sample surface was set to 30°. Based on sum rules[5], we calculated the spin and orbit moments. The m_{spin} = 1.0 μB/Fe, the $m_{orbital}$ = 0.03 μB/Fe for pure Fe_5GeTe_2; the m_{spin} = 1.1 μB/Fe, the $m_{orbital}$ = 0.06 μB/Fe for $Fe_{3.85}Co_{1.15}GeTe_2$. The direction of the spin moment and orbit moment is parallel for both centrosymmetric phases. Figure S7 shows the XMCD hysteresis loops for both Co and Fe elements of the $Fe_{2.5}Co_{2.5}GeTe_2$ at 80 K. The two curves almost overlap, showing a ferromagnetic coupling of Co and Fe. The square loops indicate an out-of-plane easy magnetization axis from the $Fe_{2.5}Co_{2.5}GeTe_2$ system.

In general, the 3*d* band of the iron in pure Fe_5GeTe_2 is more than half-filled and, thus, according to Hund's rule, the spin moment and orbital moments should be aligned parallel to each other. [6] Interestingly, the spin moment is antiparallel to the orbital moment for iron and cobalt in this non-centrosymmetric FCGT system. A comparative XMCD measurement in a $Fe_{3.85}Co_{1.15}GeTe_2$ nanoflake (centrosymmetric) was also performed and a parallel alignment of the spin and orbital moments was found. This comparison implies that the opposite direction of the spin and orbital moment in the non-centrosymmetric FCGT likely derives from the inversion symmetry breaking rather than the changing electronic structure by doping. In a previous study, the interfacial DMI in multilayer film systems closely correlated with orbital

magnetism.[7] This phenomenon may imply that the bulk DMI can induce an unusual spin-orbit interaction in this unique layered polar magnetic metal.

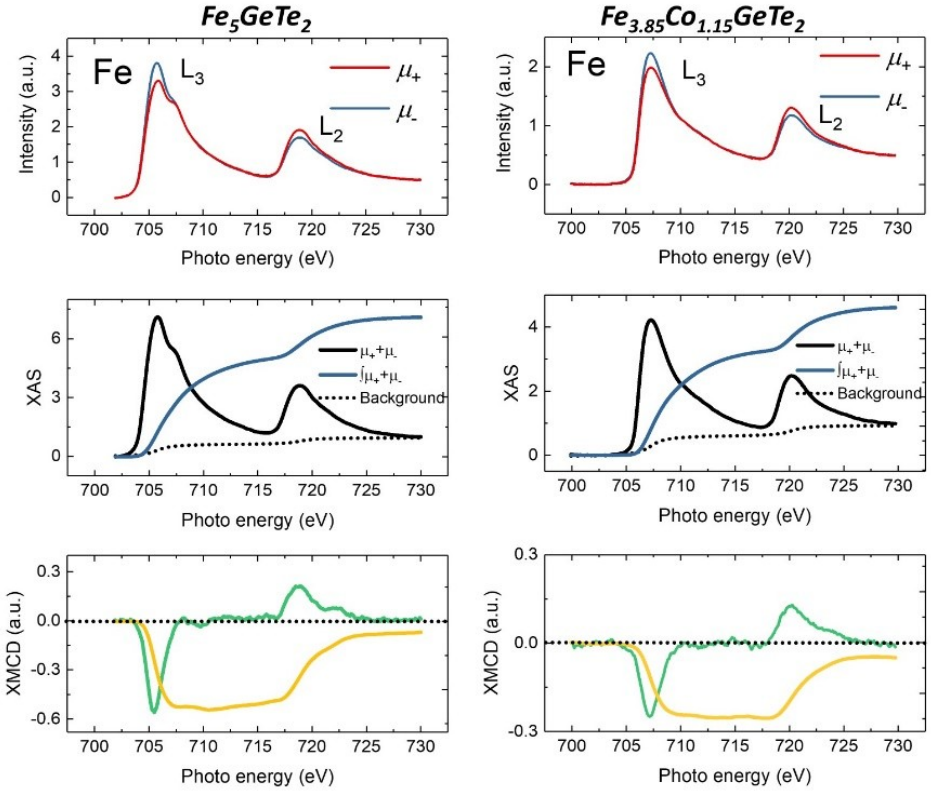

Figure S6 XAS/XMCD measurements. The XAS/XMCD spectrums were taken at 80 K under a magnetic field of 1.6 T for pure Fe_5GeTe_2 and $Fe_{3.85}Co_{1.15}GeTe_2$ nanoflake.

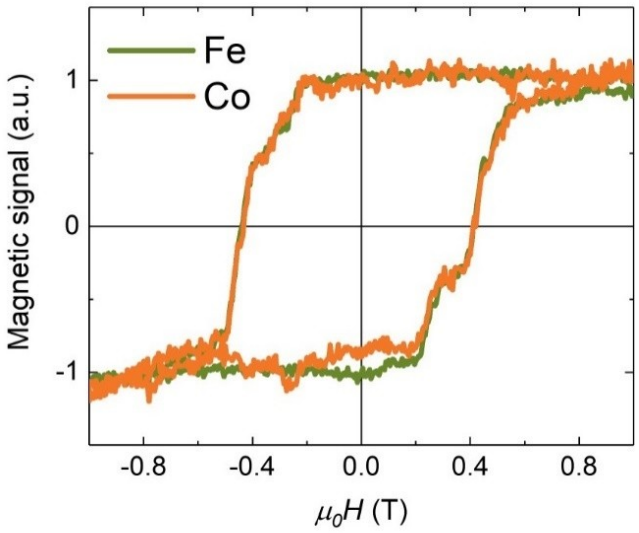

Figure S7 XMCD hysteresis loops. The magnetic-field dependent XMCD intensity for the Co and Fe elements of the $Fe_{2.5}Co_{2.5}GeTe_2$ at 80 K. The photon energy was set to the maximal XMCD signal.

6. Room-temperature current-induced magnetization switching

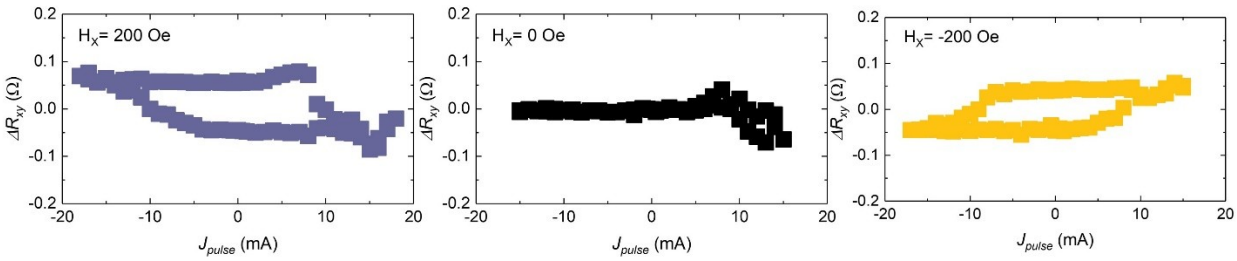

Figure S8 Room-temperature current-induced magnetization switching. ΔR_{xy} as a function of current pulses under in-plane external magnetic fields $H_X = +200$ Oe (blue), 0 Oe (black), and −200 Oe (yellow) at room temperature.

7. Joule heating effect

We compared the resistance-temperature and current curves to estimate the sample heating by Joule heating. Figure S9**a** shows the temperature-dependent resistance of the device. The measured current is d. c. with a magnitude of 0.1 mA. The resistance increases as the temperature increases. Figure S9**b** shows the current-dependent resistance of the device at room temperature. The resistance increases with the current increase due to the Joule heating of the current. We estimated that the temperature of the sample was about 343 K (330K) when we applied an 18 mA (15 mA) d.c. pulse. The FCGT nanoflake is still a ferromagnetic ground state. (see Figure 2).

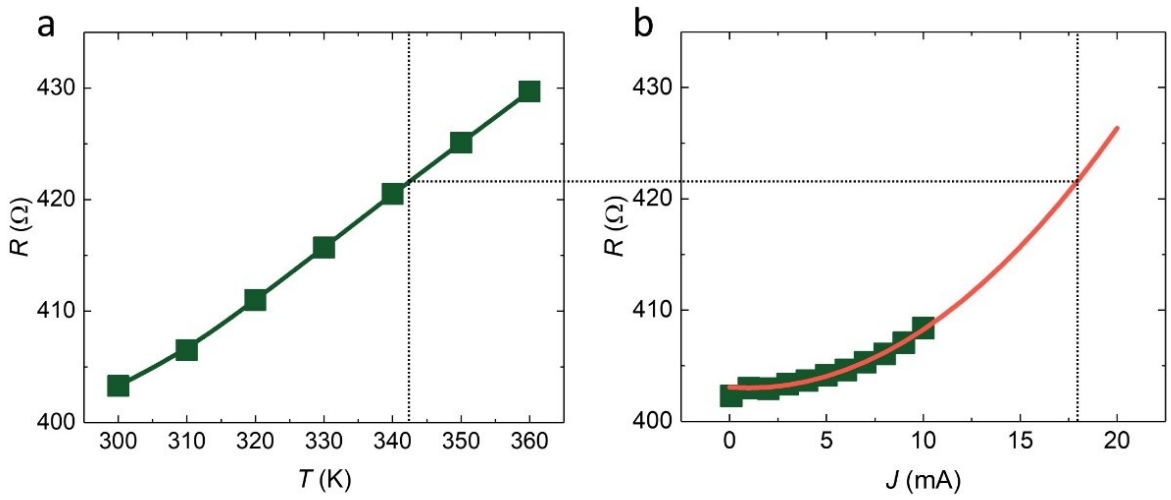

Figure S9 Joule heating effect. a) Resistance-temperature curve of the 15 L FCGT nanoflake of the device. **b**) The d. c. current dependence of resistance at room temperature.

8. Demagnetization due to the Joule heating effect

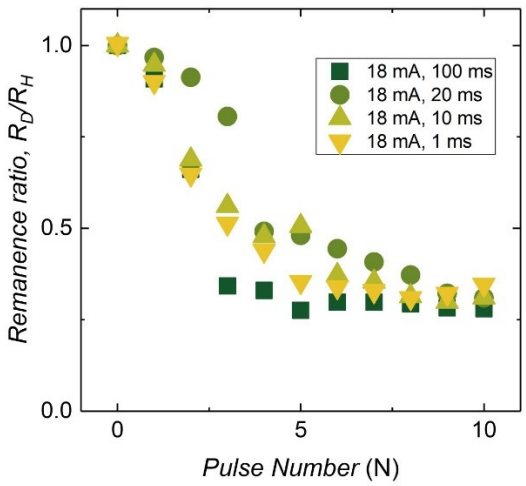

Figure S10 Demagnetization due to the Joule heating effect for various current pulse widths. Before each time applying current, the magnetization was initialized to an up-direction state with an out-of-plane magnetic field of 2 kOe. Then, we removed the magnetic field and applied a *d. c*. current with a magnitude of 18 mA for different current pulse widths (1 ms, 10 ms, 20 ms, 100 ms). After applying a current, the R_{xy} falls to ~ 20% of the saturated anomalous Hall resistance. This also was observed in Pt/Fe_3GeTe_2 [8] and $SrIrO_3$/$SrRuO_3$[9] systems.

9. The magnetization switching under in-plane external magnetic fields perpendicular to the current

We measured the current-induced magnetization switching under the in-plane external magnetic field along the *y*-direction at room temperature in Fig S11. Figure S11**a, b** show the current-dependent Hall resistance under the magnetic field of ±200 Oe. The magnetization switching disappeared. This is also confirmed by the pulse cycle measurement in Fig. S11**c**. We also checked the in-plane magnetic anisotropy by the direction of the magnetic field dependence of Hall measurements. Figure S12 shows no in-plane magnetic anisotropy of the FCGT nanoflake. These indicate that the field-like torque cannot efficiently switch the magnetization in this system and the magnetization switching did not originate from Joule heating annealing and Oersted's field. [10]

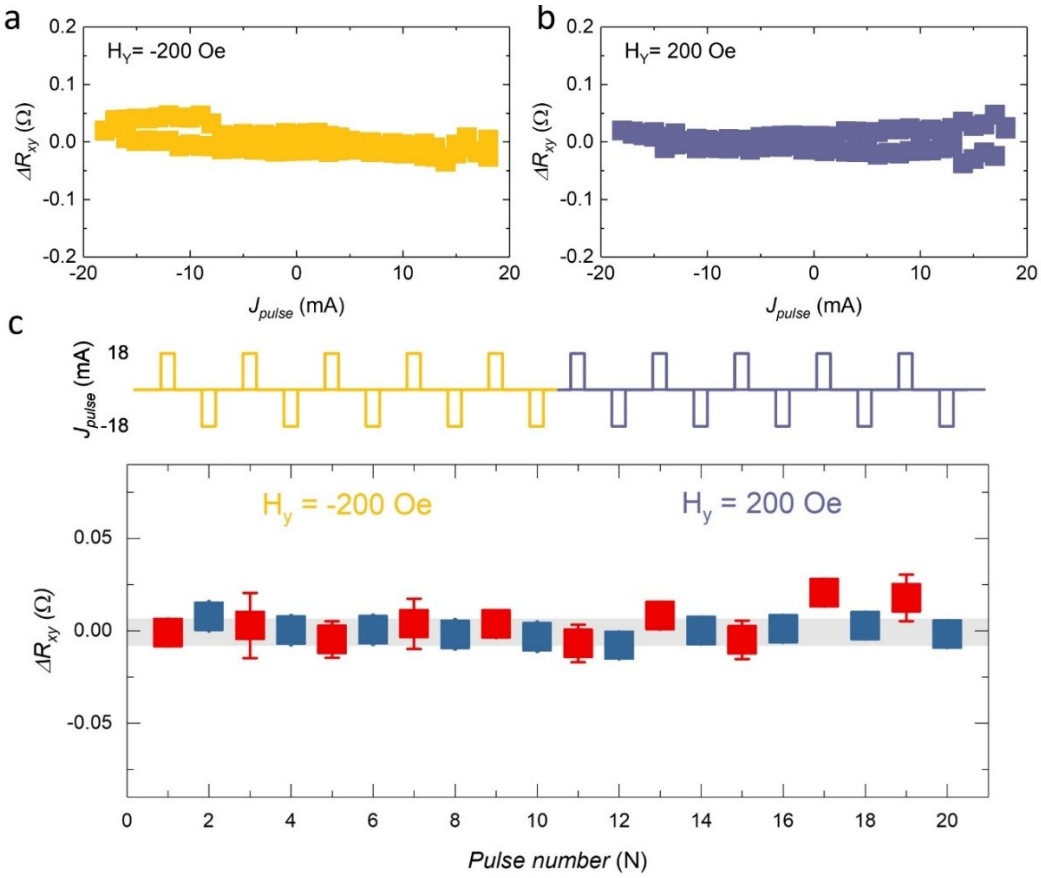

Figure S11 The magnetization switching under in-plane external magnetic fields perpendicular to the current. a), b) The Hall resistance as a function of pulse current is measured under an in-plane magnetic field along the *y*-direction with a magnitude of 200 Oe (**a**) and -200 Oe (**b**). **c**) The Hall resistance is recorded after cycle pulse current J_{pulse} = ±18 mA at different magnetic fields. The up panel shows the pulse sequence, while the low panel shows the corresponding Hall resistances.

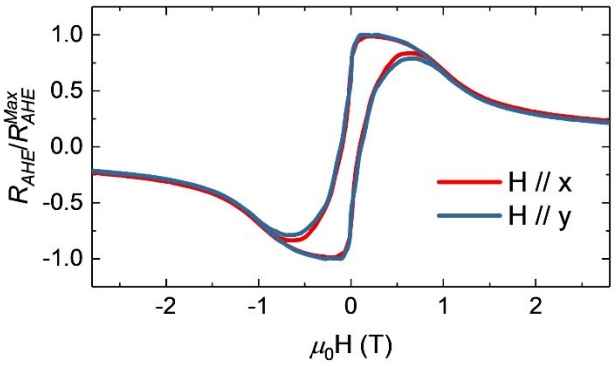

Figure S12 Magnetic anisotropy. The anomalous Hall resistance of the FCGT switching experimental device was measured along with the different directions at room temperature. The curves almost overlap, indicating no in-plane magnetic anisotropy in the 15 L thick flake FCGT.

10. Current-induced magnetization switching in thick nanoflake at low temperature

Although the thick nanoflakes exhibit a multidomain at room temperature, the strong perpendicular anisotropy drives the flake stabilization of the single-domain state as the temperature decreases. The current-induced magnetization switching in a 200-nm-thick sample can be achieved at 60 K under a ± 3600 Oe in-plane field in Fig. S13. The observation of current-induced magnetization self-switching in a 200-nm-thick FCGT nanoflake indicates that the SOT arises from the bulk inversion symmetry breaking rather than surface or interface effects.

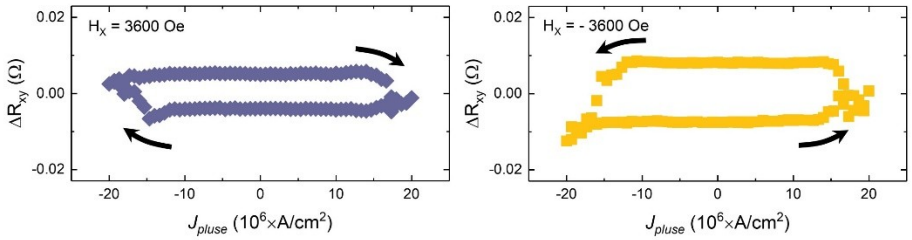

Figure S13 Current-induced magnetization switching in thick nanoflake. ΔR_{xy} as a function of current pulses under in-plane external magnetic fields $H_x = +3600$ Oe (blue), and −3600 Oe (yellow) at 60 K.

Reference

[1] H. Zhang, et al. A room temperature polar magnetic metal Phys. Rev. Mater. **6**, 044403 (2022).

[2] N. Nagaosa et al. Topological properties and dynamics of magnetic skyrmions Nat. Nanotech. **8**, 899 (2013).

[3] T. Yokouchi, et al. Emergent electromagnetic induction in a helical-spin magnet Nature **586**, 232 (2020).

[4] H. Zhang, et al. Room-temperature skyrmion lattice in a layered magnet $(Fe_{0.5}Co_{0.5})_5GeTe_2$ Sci. Adv. **8**, eabm7103 (2022).

[5]C. T. Chen, et al. Experimental Confirmation of the X-Ray Magnetic Circular Dichroism Sum Rules for Iron and Cobalt Phys. Rev. Lett. 75, 152 (1995).

[6] K. Yamagami, et al. Itinerant ferromagnetism mediated by giant spin polarization of the metallic ligand band in the van der Waals magnet Fe_5GeTe_2 Phys. Rev. B **103**, L060403 (2021).

[7] S. Kim, et al. Correlation of the Dzyaloshinskii–Moriya interaction with Heisenberg exchange and orbital asphericity Nat. Commun. **9**, 1648 (2018).

[8] X. Wang, et al. Current-driven magnetization switching in a van der Waals ferromagnet Fe_3GeTe_2 Sci. Adv. **5**, eaaw8904 (2019).

[9] L. Liu, et al. Current-induced magnetization switching in all-oxide heterostructures Nat. Nanotech. **14**, 939 (2019).

[10] K. Yasuda et al. Current-Nonlinear Hall Effect and Spin-Orbit Torque Magnetization Switching in a Magnetic Topological Insulator Phys. Rev. Lett. **119**, 137204 (2017).